



Preparation and Degradation Behavior of Composite Bio-Coating on ZK60 Magnesium Alloy Using Combined Micro-Arc Oxidation and Electrophoresis Deposition

Ze-Xin Wang¹, Lei Xu¹, Jin-Wei Zhang¹, Fei Ye¹, Wei-Gang Lv², Cheng Xu¹, Sheng Lu^{1*} and Jun Yang¹

¹ School of Materials Science and Engineering, Jiangsu University of Science and Technology, Zhenjiang, China, ² Zhenjiang Naisi Advanced Materials Co., Ltd., Zhenjiang, China

OPEN ACCESS

Edited by:

Linjiang Chai,
Chongqing University of Technology,
China

Reviewed by:

Liqiang Wang,
Shanghai Jiao Tong University, China
Hucheng Pan,
Northeastern University, China

*Correspondence:

Sheng Lu
lusheng_ktz@just.edu.cn

Specialty section:

This article was submitted to
Biomaterials,
a section of the journal
Frontiers in Materials

Received: 20 April 2020

Accepted: 22 May 2020

Published: 07 July 2020

Citation:

Wang Z-X, Xu L, Zhang J-W, Ye F,
Lv W-G, Xu C, Lu S and Yang J
(2020) Preparation and Degradation
Behavior of Composite Bio-Coating
on ZK60 Magnesium Alloy Using
Combined Micro-Arc Oxidation
and Electrophoresis Deposition.
Front. Mater. 7:190.
doi: 10.3389/fmats.2020.00190

In this work, ZK60 magnesium alloy was employed as the substrate substratum for producing micro-arc oxidation (MAO) coating which contains Ca and P. Electrophoretic deposition (ED) process was conducted on the micro-arc oxidized sample to prepare a hydroxyapatite (HA) layer on the original coating. X-ray diffraction (XRD), scanning electron microscopy (SEM), energy dispersive spectrometer (EDS) and Fourier transform infrared spectroscopy (FT-IR) were used to analyze the phase constituents and microstructures of both MAO and MAO-ED coatings. Corrosion resistance and degradation behavior of the coatings in SBF were investigated by electrochemical tests and simulated body fluid (SBF) immersion tests. The results indicate that a dense HA layer about 5 μm in thickness had been successfully prepared on the MAO coating. After going through the ED process, the porosity of the MAO-ED coating had decreased from 5.63 to 0.81%. The Ca/P ratio of the MAO-ED coating had become 1.60, which indicates a potential biocompatibility of the material. Therefore, the MAO-ED coating can induce the deposition of bioactive products from SBF. During an immersion test of SBF for 10 days, the weight gain of MAO-ED sample continued to increase, showing that the deposition rate of the induced products is always higher than that of corrosion products before experiencing the 10 days of immersion. The deposition of induced products protects the substrate from being corroded so effectively that it ensures the good mechanical properties and biocompatibility during the initial stage of implantation. According to the changes in sample morphologies and the electrochemical measurements in SBF, a relevant degradation model has been suggested and the underlying mechanism for degradation behavior is discussed.

Keywords: magnesium alloy, micro-arc oxidation, electrophoretic deposition, composite coating, HA, degradation behavior

INTRODUCTION

With the development of modern medical science, there are more user-friendly and diversified choices for biomedical materials (Liu et al., 2015; Ataee et al., 2017; Zheng et al., 2017; Chen J. et al., 2019; Qin et al., 2019; Zhang and Chen, 2019; Zhang et al., 2020). New composite materials with biomedical purposes have attracted a lot of attention. Mg alloys, as one of the biomedical materials, possess numerous advantages such as biodegradation, similar density and modulus to bones, reliable bone induction (Zhang et al., 2006a,b; Razavi et al., 2014; Qin et al., 2015; Peng et al., 2016; Cipriano et al., 2017; Chai et al., 2018; Rabadia et al., 2019; Zhang Y.M. et al., 2019). Such advantages can avoid a secondary surgery for patients to remove their implants and get rid of the “stress shielding effect.” In this way Mg alloys can improve the growth and aggradation of new bone tissue. Hence, the investigation of Mg alloys has been highlighted in the field of biodegradable materials (Agarwal et al., 2017; Bian et al., 2018; Chen C. et al., 2018). The development of biodegradable magnesium has completely changed the concept of metallic biomaterials. As a qualified magnesium alloy implant, the corrosion rate of it should match that of the tissue healing and the biocompatibility should be acceptable. Furthermore, it also should possess sufficient mechanical properties. Mechanical properties of a magnesium alloy implant greatly depend on the grain size, the solubility of alloying elements and the size, amount and distribution of the second phase (Li and Zheng, 2013; Pan et al., 2018). Therefore, the composition, the heat-treatment and processing technique of the magnesium alloy have become a hot issue. Currently, there are some scholars who have employed non-toxic or low toxic elements and developed a new type of magnesium alloy. Among them, Mg-Ca alloy has been extensively applied in different fields. Calcium is a major component in human bone and is essential in chemical signaling with cells (Ilich and Kerstetter, 2000). Magnesium is necessary for the calcium incorporation into the bone (Serre et al., 1998), which might be expected to be beneficial to the bone healing with the co-releasing of Mg and Ca ions, moreover, Ca ion can help to refine grain. Pan et al. successfully developed a light-weight Mg–1.0Ca–1.0Al–0.2Zn–0.1Mn extrusion alloy and Mg–2Sn–2Ca alloy with high strength–ductility synergy (Pan et al., 2019, 2020).

However, the corrosion resistance of Mg alloy is poor and the rate of its degradation in the practical application is too fast, which vastly shortens its service period. All these deficiencies have greatly limited clinical applications of Mg alloys. Therefore, it is necessary to design new kinds of Mg alloys with improved corrosion resistance and longer degradation period (Jiang et al., 2016; Zhu et al., 2017; Zhang L.C. et al., 2019). Micro-arc oxidation (MAO) is an advanced anodizing technique that generates *in situ* ceramic-like coatings via high voltage discharge, which is controlled by the electrical parameters of process and the compositions of electrolyte (Pezzato et al., 2015; Xiong et al., 2017). The previous works show that the corrosion resistance of Mg alloys can be effectively improved by MAO (Gu et al., 2013; Jia et al., 2014; Chen et al., 2017; Wang et al., 2018). It is well known that MAO coatings have a porous structure and can easily be permeated by corrosive species (e.g., Cl^-), which results

in their bad corrosion resistance. On the other hand, it is hard to trigger bone induction and meet the requirements of clinical applications with such a small number of the contents of Ca and P in MAO coatings. Hence, the key to endow the coatings with excellent biocompatibility and bioactivity is the re-designation of MAO coatings (Shadanbaz and Dias, 2012; McEntire et al., 2015; Wang et al., 2019; Xia et al., 2020).

As an important part of bone tissue, hydroxyapatite (HA) has gradually become an essential biological medium in the process of surface modification of Mg alloys. HA, chemical formula of $\text{Ca}_{10}(\text{PO}_4)_6(\text{OH})_2$, has good biocompatibility for its production of non-toxic substances in the body and reliable bone induction to promote the growth of new bone cells. Research has shown that a good bone tissue growth can be found along the surface or the interior void of the implants coated by HA (Suchanek and Yoshimura, 1998; Tampieri et al., 2001; Habibovic et al., 2002; Kim et al., 2004; Bose et al., 2015). However, the pure HA is unable to be directly used as an implant owing to its poor mechanical properties such as high brittleness and low strength. As a result, it is of great importance to use HA to produce a synthesis of composite coating which combines biological activity, bone induction and good mechanical properties for biomedical application (Chen G. et al., 2016). So far, there are many surface modification methods for applying HA to the surfaces of metals and alloys. Electrophoretic deposition (ED) (Hornberger et al., 2012; Sankara Narayanan et al., 2014) is a surface modification method for depositing particles on a substrate in a suspension under electric field forces.

It has been reported that HA coatings can be prepared on the micro-arc oxidation coatings by electrophoretic deposition. Xiong et al. (2017) argued that by comparison, the MAO-ED composite coating has stronger bioactivity and ability to be protected long-term than the MAO coating and the n-MAO coating. Razavi et al. (2015) modified the surface of Mg implants by means of fluoridated hydroxyapatite (FHA: $\text{Ca}_{10}(\text{PO}_4)_6\text{OH}_x^{2-\text{F}_x}$) through the combined MAO and ED techniques. The results revealed a significant enhancement in the biocompatibility of FHA/MAO coated implant compared to the uncoated one according to the *vivo*. So far, there are still few works on the production of composite coatings by combining MAO and ED as well as their degradation characteristics in simulated body fluid (SBF). The degradation behavior of MAO-ED composite coatings directly determines their qualities of the implants in human body. Therefore, it is significant to investigate the degradation behavior of MAO-ED composite coatings in order to better understand the characteristics of the materials.

In our previous work, the degradation behavior of ZK60 MAO coating has been deeply investigated (Wang et al., 2018). An anti-corrosion layer that contains Ca and P was synthesized on ZK60 Mg alloy by MAO technology based on the perspective of improving the corrosion resistance and bioactivity of Mg alloy matrix. In this work, bioactive HA layer was produced by ED on MAO coating. X-ray diffraction (XRD) and scanning electron microscopy (SEM) were employed to analyze phase constituent and microstructural characteristics of composite coatings. Based on the corrosion tests and electrochemical measurements, the

degradation behavior of composite coatings was systematically investigated and the relevant degradation model was established.

MATERIALS AND METHODS

Preparation of MAO Coating

Commercially available rolled ZK60 Mg alloy ZK60 Mg alloy (Mg-5.8wt%Zn-0.45wt%Zr) was cut into 20 mm × 20 mm × 5 mm bulks as for the substrates. MAO was conducted in the optimized electrolyte which composed of 0.8 g/L (NaPO₃)₆, 6 g/L Na₂SiO₃·9H₂O, 0.5 g/L Ca(CH₃COO)₂·H₂O, 0.5 g/L NaH₂PO₄·H₂O and 2.8 g/L NaOH. Current density, duration time, positive duty cycle, negative duty cycle and frequency were set as 10 A/dm², 13 min, 40, 60, and 500 Hz, respectively.

Preparation of ED Coating

For the electrophoretic deposition, HA powder with an average particle size of 15 nm and Ca/P ratio of 1.64 was chosen then was dried at 200°C for 3 h to remove water molecules before the process. An anhydrous alcohol based on HA (10 g/L) slurry with an adequate addition of concentrated nitric acid (to keep the slurry pH at 3~4 and also to avoid agglomeration of HA particles) was prepared and used in electrophoreses cell for the deposition of HA layers on MAO coatings so as to obtain the MAO-ED composite coatings. The slurry was subjected to ultrasonic oscillation for 1 h to ensure its uniformity and stability followed by a 24 h standing before electrophoretic deposition.

WWL DC voltage stabilizer was applied as the power to supply for the ED process. A 40 mm × 30 mm × 2 mm stainless steel was applied as an anode and the micro-arc oxidized Mg bulk was used as the cathode. By means of adjusting the voltage and time of electrophoretic deposition, MAO-ED coating was produced. Deposition voltage and deposition time were set as 90 V and 2 min. To ensure the uniformity of the solution, a constant temperature magnetic stirrer was used during the whole ED process. When the ED process was over, the power was turned off and the sample was taken out. Then the electrophoretic deposited sample was dried and sintered in the furnace at 200°C for 1 h and cooled in the furnace.

Characterizations

JSM-6480 scanning electron microscope equipped with energy-disperse spectroscopy (EDS) was used for microstructure characterization. Phase constituents were collected by X-ray diffraction by means of a Shimadzu XRD-6000 with CuK_α radiation operated at 40 kV. The parameters of 2θ range of 20°–80° and scan rate of 4°/min were employed in this work. Fourier transform infrared spectroscopy (FT-IR) spectra were recorded through fourier transform infrared spectrometer FT2000 between the frequency range of 4,000 and 500 cm⁻¹. Image J software was used to calculate the coating porosity (Chen L.Y. et al., 2019). Electrochemical impedance spectroscopy (EIS) was performed on a CS2310 electrochemical workstation (CorrTest, Wuhan, Hubei, China) at a frequency ranging from 100 mHz to 100 kHz with a low alternating current amplitude

of 5 mV in SBF at 37°C. ZSimp WIN software was used for fitting the EIS data.

SBF Immersion Test

A series of 20-day immersion tests in SBF were conducted by use of MAO-ED samples in a thermostat water bath at 36.5 ± 0.5°C. 1,000 ml SBF with ion concentrations which are similar to the ones in human blood (Table 1) was prepared by dissolving reagents (Table 2) into distilled water. Tris and HCl were used to adjust the pH value to 7.45. A Banter-920-UK precision pH meter was used to measure the pH of SBF.

The pre-weighed samples (three parallel samples as a group for each immersion period) were soaked in the solution at 36.5 ± 5°C with the volume (cm³) 10 times to its total surface area (cm²). The SBF solution was changed and the pH value was recorded every 24 h. A group of samples was taken every 5 days. After being rinsed and dried, it was weighed again. The weight gain R_{wt} can be calculated as the below equation (Chen et al., 2015b; Chen L. et al., 2016; Yazdimamaghani et al., 2015):

$$R_{wt} = (M_1 - M) / M \times 100\% \quad (1)$$

where M (g) indicates the sample weight before immersion and M_1 (g) indicates the sample weight after immersion.

RESULTS AND DISCUSSION

Microstructures of MAO Coating and MAO-ED Coating Surface Morphology

Figures 1a,b shows the surface micro-morphologies of the MAO coating and the MAO-ED composite coating. It can be seen that uniformly distributed micro-pores, melts and micro-cracks have appeared on the MAO coating surface (Figure 1a). Meanwhile, there are also many visible crater-like channels on the MAO coating surface. During the MAO process, the instantaneous high-energy caused by discharge sparks repeatedly break down the oxidized coating which is formed on substrate surface, resulting in a lot of melts around the breakdown channels. Under the synergistic effect of high temperature and pressure, complex electrochemical reactions take place between the melts and the solution in the channels, causing the deposition of MgO and other calcium/phosphor salts on the channel inwall and around the channel openings. When the melts are exposed to the electrolyte, the quenching process can cause thermal stress, resulting in the formation of micro-cracks (Zhou et al., 1999; Chen et al., 2010a,b, 2015a; Liu et al., 2010).

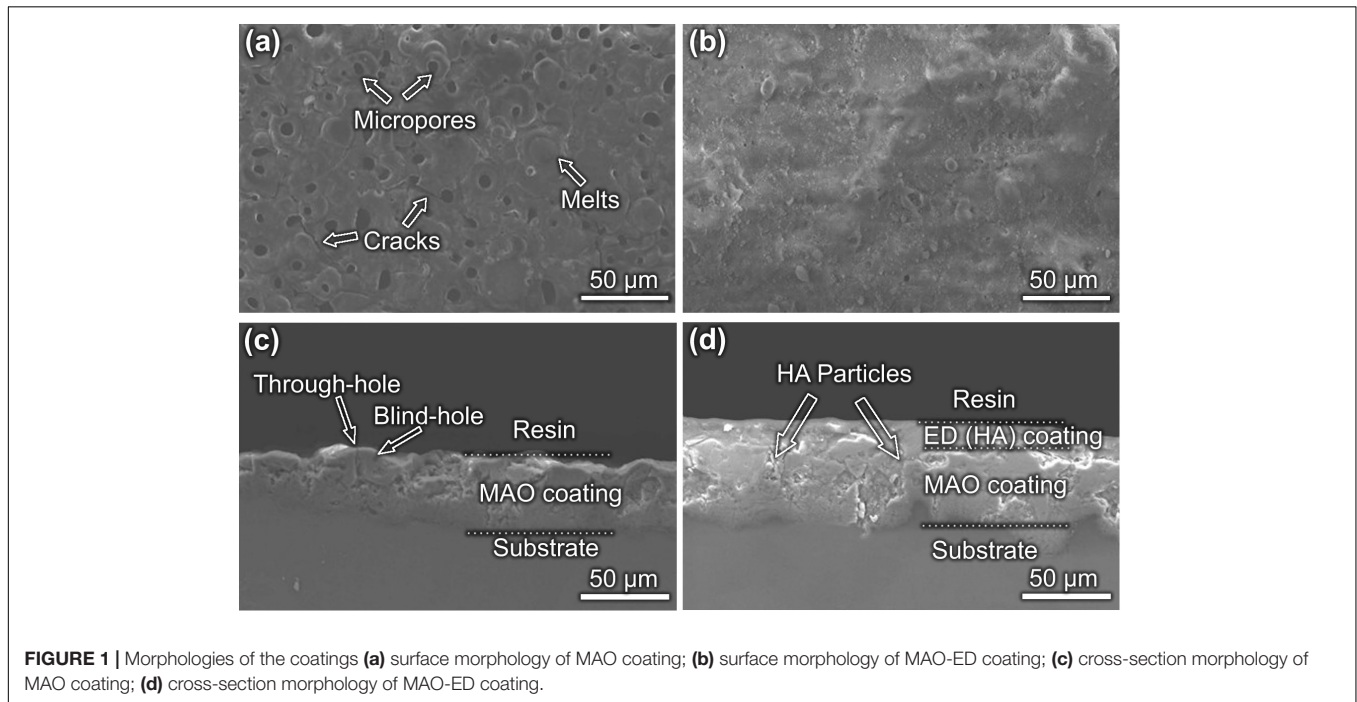
After the ED process, a new ED coating with few micro-pores and/or micro-cracks can be observed on the surface of the

TABLE 1 | Ion concentration of simulated body fluid (SBF) and blood plasma (m mol/L).

	Na ⁺	K ⁺	Mg ²⁺	Ca ²⁺	Cl ⁻	HCO ₃ ⁻	HPO ₄ ²⁻	SO ₄ ²⁻
SBF	142.0	5.0	1.5	2.5	148.8	4.2	1.0	0.5
Blood plasma	142.0	5.0	1.5	2.5	103.0	27.0	1.0	0.5

TABLE 2 | Reagents and dose for 1,000 ml SBF.

Reagent	NaCl	NaHCO ₃	KCl	K ₂ HPO ₄ ·3H ₂ O	MgCl ₂ ·6H ₂ O	Ca ₂ Cl	Na ₂ SO ₄	1.0 M-HCl
Dosage (g)	8.035	0.355	0.225	0.231	0.311	0.278	0.072	39 ml

**FIGURE 1** | Morphologies of the coatings (a) surface morphology of MAO coating; (b) surface morphology of MAO-ED coating; (c) cross-section morphology of MAO coating; (d) cross-section morphology of MAO-ED coating.

sample (**Figure 1b**). The surface porosity of the MAO-ED coating decreases from 5.63% (before the ED process) to 0.81% for that the MAO coating with high porosity offers considerable sites for the growth of HA. Nano-sized HA-rods are easily accommodated and developed in the micro-pore at the early stage of ED. The porous layer is gradually covered by the deposition layer with the increase of treatment time. In this way, the porosity decreases after the ED process (Gao et al., 2011; Xiong et al., 2014), indicating that the micro-pores and micro-cracks are effectively blocked by the ED coating, which leads to a smoother and denser sample surface. Based on the EDS analysis, it is found that the Mg content of the coating decreases while the contents of Ca and P have increased after the ED process (**Table 3**). The Ca/P ratio of the MAO-ED coating surface is 1.60, which is very close to that of the HA powder used in the experiment (O: 67.78 at%; Ca: 20.02 at%, P: 12.20 at%) (Meng et al., 2011; Bakhsheshi-Rad et al., 2014).

Wettability is an important factor to evaluate the biocompatibility of biomaterials. Cells prefer to adhere to and grow on hydrophilic surfaces, that is, the higher the

wettability is, the better the cell compatibility will be (Gu et al., 2013). When the contact angle of water to the material surface is less than 80°, cells can adhere to and grow on the surface (Gu et al., 2013). The contact angle of water to the MAO-ED coating is 0°, making the water easy to spread out on the surface completely. Hence, owing to the good wettability, the MAO-ED composite coating is expected to have a better biocompatibility and bioactivity (Pan and Yoon, 2018).

Cross-Sectional Morphologies and Element Distributions

Figures 1c,d shows the cross-sectional morphologies of MAO coating and MAO-ED coating. Both through-holes and blind-holes can be observed on MAO coating (**Figure 1c**). Corrosive media like Cl⁻ can permeate into the coating easily through the through-holes so that the substrate can be corroded quickly. Fortunately, the loose and porous surface of MAO coating meets the requirements of electrophoretic deposition (insulating, uniform, and porous). The micro-pore grooves provide preferable positions for the deposition of HA particles. Therefore, a considerable number of HA particles enter into the MAO coating through the through-holes (as indicated by arrows in **Figure 1d**), resulting in the formation of a mechanical bond interface between ED coating and MAO coating. Hence, HA particles will not easily fall off from the surface of the sample. The other HA particles deposit on the MAO coating surface. The deposited HA layer with a thickness of about 5 μm is uniform

TABLE 3 | Element contents of the coatings on ZK60 Mg alloys derived from EDS analysis (at%).

Coatings	Mg	O	Ca	P	Si
MAO coating	31.27	60.69	1.05	2.41	4.58
MAO-ED coating	0.53	63.71	21.99	13.77	-

and dense (**Figure 1d**). Such a flawless coating can provide a good barrier against the invasion of corrosive ions, which is consistent with the results shown in **Figures 1a,b**.

Figure 2 shows the element distributions of Mg, Ca and P in MAO coating and MAO-ED coating. Due to the existence of micro-pores and micro-cracks, discontinuous element distributions are observed in MAO coating. After the ED process, one can observe that a layer with higher Ca-P content is formed and covers the original MAO coating surface. From the enlarged view of the through-hole position (as shown by an arrow), Ca and P are embedded in the hole, verifying that the micro-pores have been sealed.

Analysis of Phase Constituent

XRD patterns of MAO coating and MAO-ED coating are shown in **Figure 3A**. MAO coating mainly consists of Mg, MgO, silicates and phosphates, while the MAO-ED coating is mainly made up of MgO and HA. The existence of HA peaks illustrates that the deposited HA particles form an intact and dense layer on the MAO coating surface. However, even though the HA diffraction peaks in the XRD pattern of MAO-ED coating are well matched with HA standard diffraction peaks, it is still not sufficient evidence to prove the existence of HA deposition on the surface of MAO coating. HA in solutions, especially acidic solutions with low pH values, usually forms a thermally unstable intermediate phase of octacalcium phosphate ($\text{Ca}_8\text{H}_2(\text{PO}_4)_6 \cdot 5\text{H}_2\text{O}$, OCP) (Burg et al., 2000; Han et al., 2003). The crystal structure of OCP is very similar to that of HA, which has almost identical diffraction peaks within $20^\circ \sim 40^\circ$ of 2θ . It's difficult to effectively distinguish these two calcium phosphate salts by XRD. Therefore, FT-IR was employed to further confirm the phase constituent of coatings.

Figure 3B is a comparison of FT-IR patterns between HA powder and MAO-ED coating. It can be observed that compared to those of HA powder, there is no change in relevant peak positions like the asymmetric stretching vibration absorption peak of PO_4^{3-} near $1,033 \text{ cm}^{-1}$, the bending vibration absorption peaks of PO_4^{3-} near 603 and 631 cm^{-1} , and the vibration absorption peak of OH^- near $3,424 \text{ cm}^{-1}$. Each peak of MAO-ED coating is sharper than that of HA, indicating a high crystallinity of MAO-ED coating. However, the position and width of peaks of HA powder and MAO-ED coating are almost the same as each other, illustrating there is no phase transformation of HA after the ED and sintering process.

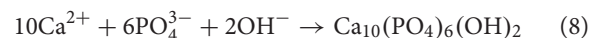
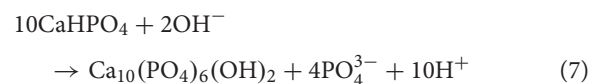
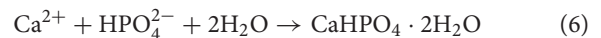
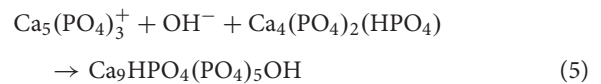
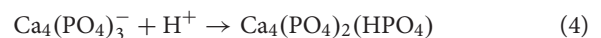
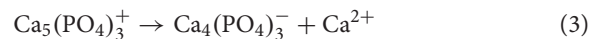
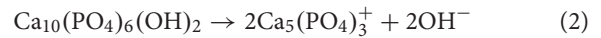
Degradation Behavior of MAO-ED Coating

SBF pH and Weight Gain of Samples

Figure 4 shows the variations of SBF pH values and weight gain of samples vs. immersion time. As shown in **Figure 4A**, the solution pH experiences a shape of 'A' change during the first 2 days, followed by a slow increasing period until the end. According to the study of García Rodenas et al. (2005), it can be inferred that ionization equilibrium reactions as shown from Eqs 2–5 and synthesis reactions as shown from Eqs 6–8 take place during the immersion (Wang et al., 2019).

At the beginning of immersion, the decomposition of the deposited HA layer produces a lot of OH^- (as shown in Eq. 2),

leading to a fast increase of pH value. With the increase of Ca^{2+} and PO_4^{3-} , Ca-P compounds are deposited while some ions of OH^- in SBF are consumed (as shown in Eqs 3–5), leading to the decrease of pH value. During the 20 days of immersion, the decompositions of HA layer and the deposition of immersion products take place simultaneously. Hence, the pH value maintains a slow growth.



According to the discussion above, the composite coating with a Ca/P ratio of 1.60 (similar to that of HA) makes it easy to induce Ca^{2+} and PO_4^{3-} in SBF and cause deposition on the coating surface (Yanovska et al., 2012). Therefore, the damage of solution to substrate was mitigated. During 20 days of immersion, the weight gain of samples increases at first and then decreases 15 days later (**Figure 4B**). It shows that the deposition of immersion products is the main reaction as compared with the degradation of MAO-ED coating at the early stage of immersion, causing the obvious weight gain of samples. At the late stage of immersion, the inducing ability decreases due to the deposition layer becoming thicker. At that time, the degradation of MAO-ED coating became the main reaction instead of the deposition of immersion products. Therefore, the weight gain of samples has decreased. However, the coating is still not completely decomposed, which effectively protects the substrate from the ingress of corrosive media and ensures the good mechanical properties and biocompatibility in the early stage of implantation. In the previous work, the degradation rates of MAO coating and Mg alloy were studied (Wang et al., 2018). It showed that after a 20-day immersion, the weight-loss rate of MAO coating reached 12% and the weight-loss rate of Mg alloy substrate reached 35% while the weight gain rate of MAO coating was 0.02%. It is the deposition of HA layer that effectively repairs the micro-pores and micro-cracks on the surface of the MAO coating and greatly improves the degradation rate of the coating. After the deposition, the MAO-ED coating possessed good biocompatibility and bioactivity, which is able to induce the growth of bone (Bose et al., 2015). The new bone can grow from the junction of the HA implant and original bone and can develop along the surface or internal space of the implant. Therefore, MAO-ED coating is in the state of weight gain during the whole immersion process.

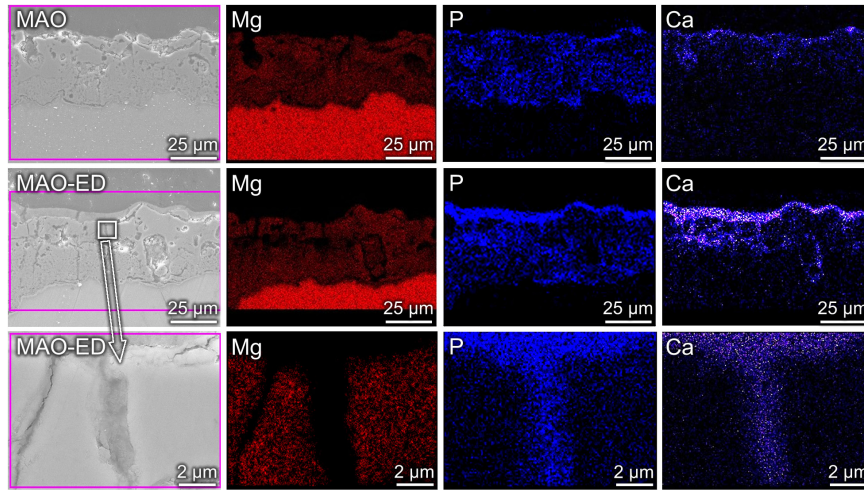


FIGURE 2 | Element distributions of MAO coating and MAO-ED coating.

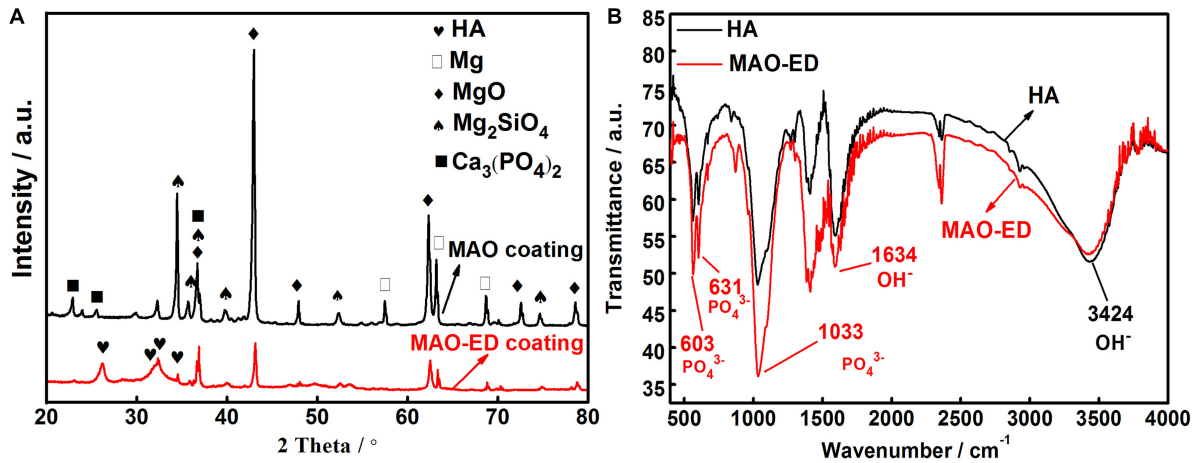


FIGURE 3 | XRD patterns of MAO coating and MAO-ED coating (A) and FT-IR of HA and MAO-ED coating (B).

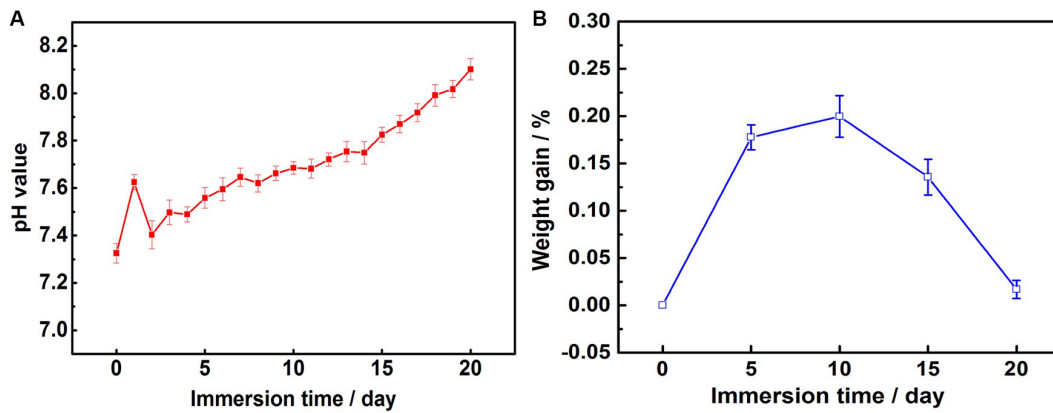


FIGURE 4 | Results of immersion tests: (A) variations in pH value of the SBF over time and (B) weight gain of MAO-ED samples after SBF immersions.

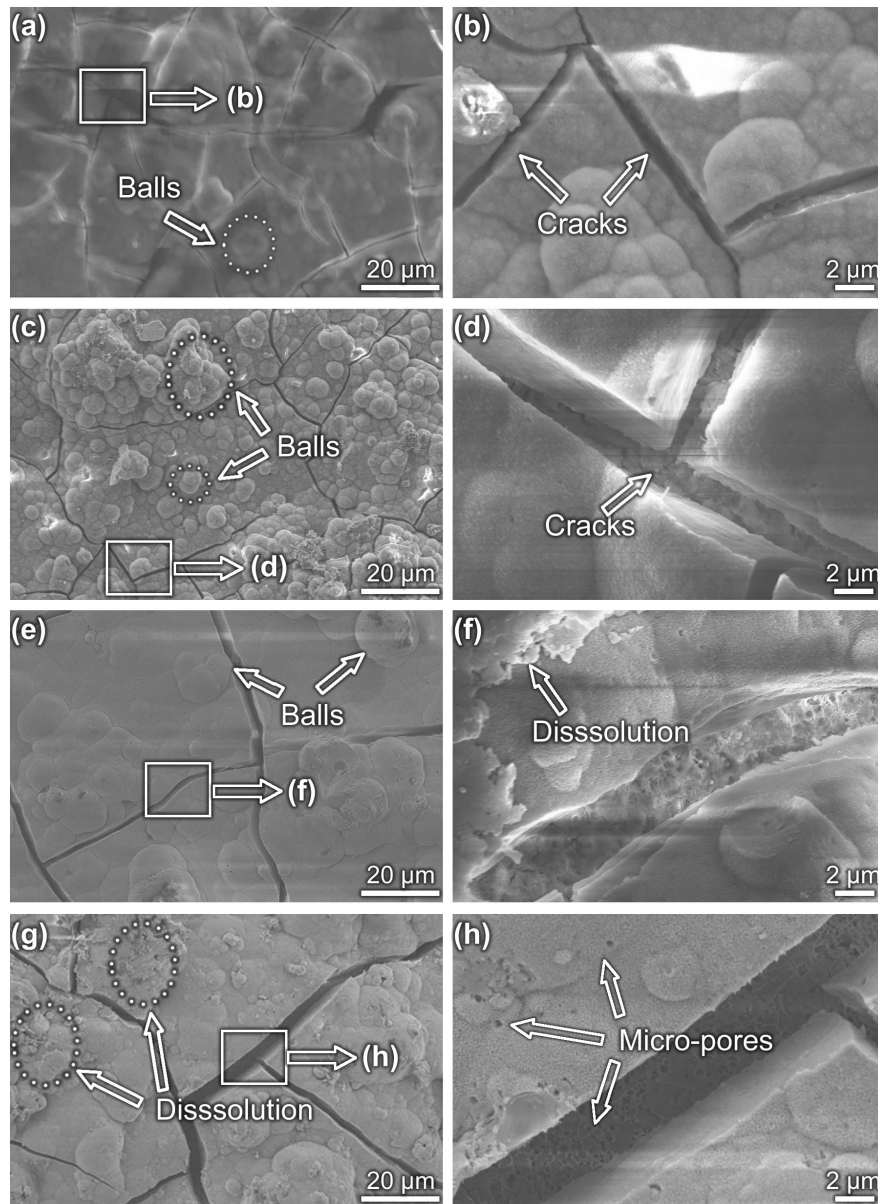


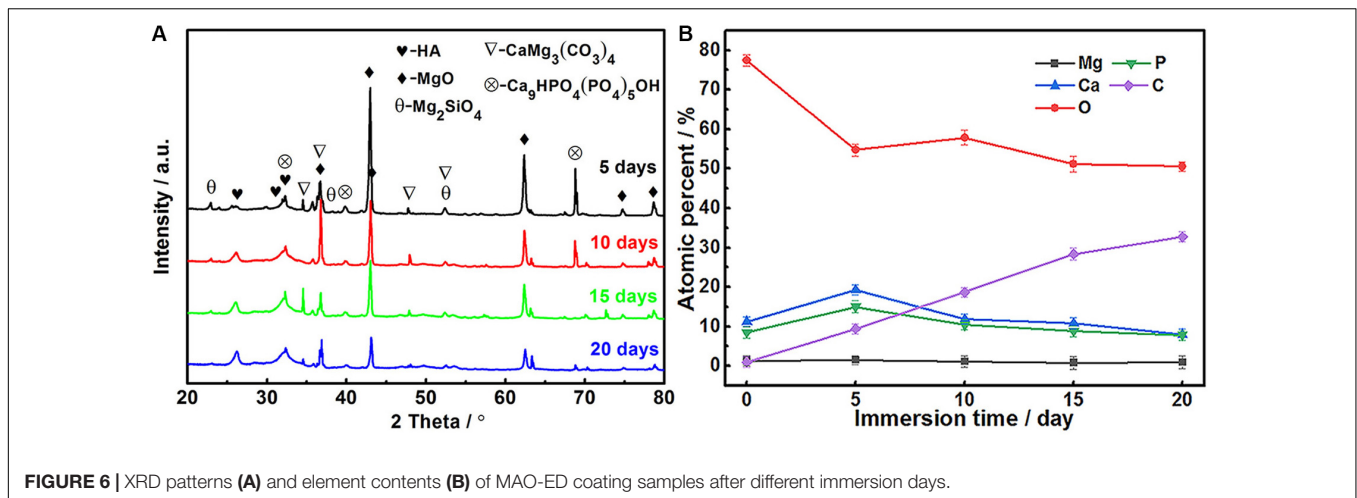
FIGURE 5 | Morphologies of MAO-ED coating samples after different immersion days: (a,b) 5 day, (c,d) 10 day, (e,f) 15 day and (g,h) 20 day.

Surface Morphologies and Element Contents

Coating surface morphology varies a lot at different immersion times (Figure 5). Some ball-like deposits as well as some micro-cracks (as shown by the arrow in Figures 5a,b) can be observed to be stacked on the surface after 5-day immersion. The Ca/P ratio of the MAO-ED coating is 1.69 after a 5-day immersion, which is higher than that of the original MAO-ED coating (1.60). After 10 days of immersion, ball-like deposits cover the surface of the sample and some deposits are agglomerated (Figures 5c,d). Meanwhile, the micro-cracks on the surface further expand and divide the surface into many polygonal plates. According to Figure 6A, the main phases of the sample surface after the 10-day immersion are MgO, $\text{CaMg}_3(\text{CO}_3)_4$, $\text{Ca}_9\text{HPO}_4(\text{PO}_4)_5\text{OH}$ and

HA, among which $\text{CaMg}_3(\text{CO}_3)_4$ and $\text{Ca}_9\text{HPO}_4(\text{PO}_4)_5\text{OH}$ are the deposits.

Many researchers believe that the micro-cracks on the MAO coatings result from the volume-shrinking effect, which is caused by the loss of moisture during the drying process (Li Y. et al., 2014; Liu et al., 2014; Agarwal et al., 2016). However, this statement cannot explain this phenomenon completely. The generation and propagation of micro-cracks are also related to the local corrosion. The uneven thickness of HA layer leads to the local corrosion and the inconstant degradation rate during immersion (Zhao et al., 2013). With the increase of immersion time, the corrosion areas gradually increase, leading to the expansion and deepening of micro-cracks. Then micro-cracks



connect to each other and gradually divide the coating into small pieces, which ultimately leads to the failure of the coating.

After the 15-day immersion, there are fewer ball-like deposits but wider micro-cracks on the sample surface (Figure 5e). Some deposits are observed to be dissolved (Figure 5f). After 20-day immersion, small fresh ball-like deposits are still presented on the sample surface (Figures 5g,h). However, the degradation products have obviously increased. Broadened micro-cracks as well as micro-pores are observed (Figures 5g,h). Based on the EDS examination, Ca and P contents on coating surfaces after different days of immersion are listed in Table 4. It can be drawn from Table 4 that the Ca/P ratio of coating surface decreases as the immersion time increases, indicating the weakening of the potential osteoinductivity.

The XRD patterns of soaked coatings (Figure 6A) show that the diffraction peaks of MgO, $\text{CaMg}_3(\text{CO}_3)_4$ and $\text{Ca}_9\text{HPO}_4(\text{PO}_4)_5\text{OH}$ weaken as the immersion time increases. In comparison, the diffraction peak of HA apparently intensifies. According to the analysis of decomposition products during immersion by García Rodenas et al. (2005) and Wang et al. (2019), it can be inferred that the deposition rate of Ca-P products induced by the HA layer gradually increases, hence the deposition product layer becomes thicker, covering the original HA layer. However, with the thickening of the deposition products, some parts of the HA layer are covered and isolated from SBF. Hence the deposition rate decreases. When the deposition rate is lower than the decomposition rate, the weight gain of the sample decreases (as shown in Eqs 6–8).

TABLE 4 | Ca and P contents on coating surface after different immersion days.

Sample (days)	Element (at%)		
	P	Ca	Ca/P
5	9.62	16.22	1.69
10	8.85	10.85	1.23
15	4.98	5.84	1.17
20	10.38	11.69	1.13

The changes in the atomic percentage of the elements on the MAO-ED coating surface during immersion are shown in Figure 6B. The original MAO-ED coating contains Ca, P and O, which are the main compositions of the HA layer. Since the MAO coating has been covered by the deposited HA layer after the ED process, Mg can hardly be detected during the immersion. C content monotonically increases during the immersion, specifying the increasing amount of carbonate deposits on the sample surface. Ca and P contents increase during the first 5 days, indicating that the increased deposits contain Ca and P, which is consistent with the above analysis. During the latter 15 days of immersion, Ca and P contents decrease to relatively stable values. By comparing the variations of Ca and P with that of C, it indicates that the dissolution and deposition of immersion products take place simultaneously.

Cross-Sectional Microstructures

Figure 7 shows the cross-sectional morphologies and element distributions of MAO-ED coating at different days of immersion. After the 5-day immersion, a Ca- and P- enriched deposition layer with a thickness of $\sim 8 \mu\text{m}$ is observed on the coating surface (the first row of Figure 7). As mentioned above, a large amount of Ca and P are also presented in the micro-pores of the MAO coating and the thickness of the ED coating is about $5 \mu\text{m}$ (Figure 2), which indicates that a dense and uniform corrosion product layer is deposited on the ED coating. After a 10-day immersion, the corrosion product layer becomes thicker, however, micro-cracks and decomposition of deposits are observed at some regions (the second row of Figure 7). After a 20-day immersion, larger-sized micro-cracks and micro-pores on and in the coating (Figures 5g,h, 7) result in the imperfections caused by the corrosion of the product layer, accelerating the degradation of the MAO-ED coating. Similar to other materials, the MAO-ED coating can be corroded due to the permeation of SBF solution through micro-cracks and micro-pores (Qin et al., 2017; Chen L.Y. et al., 2018; Sang et al., 2019; Zhang L. et al., 2019). However, the deposits are still thick enough to prevent SBF solution from completely corroding the MAO-ED coating (Luo et al., 2008; Gu et al., 2012). It has been reported that if the coating

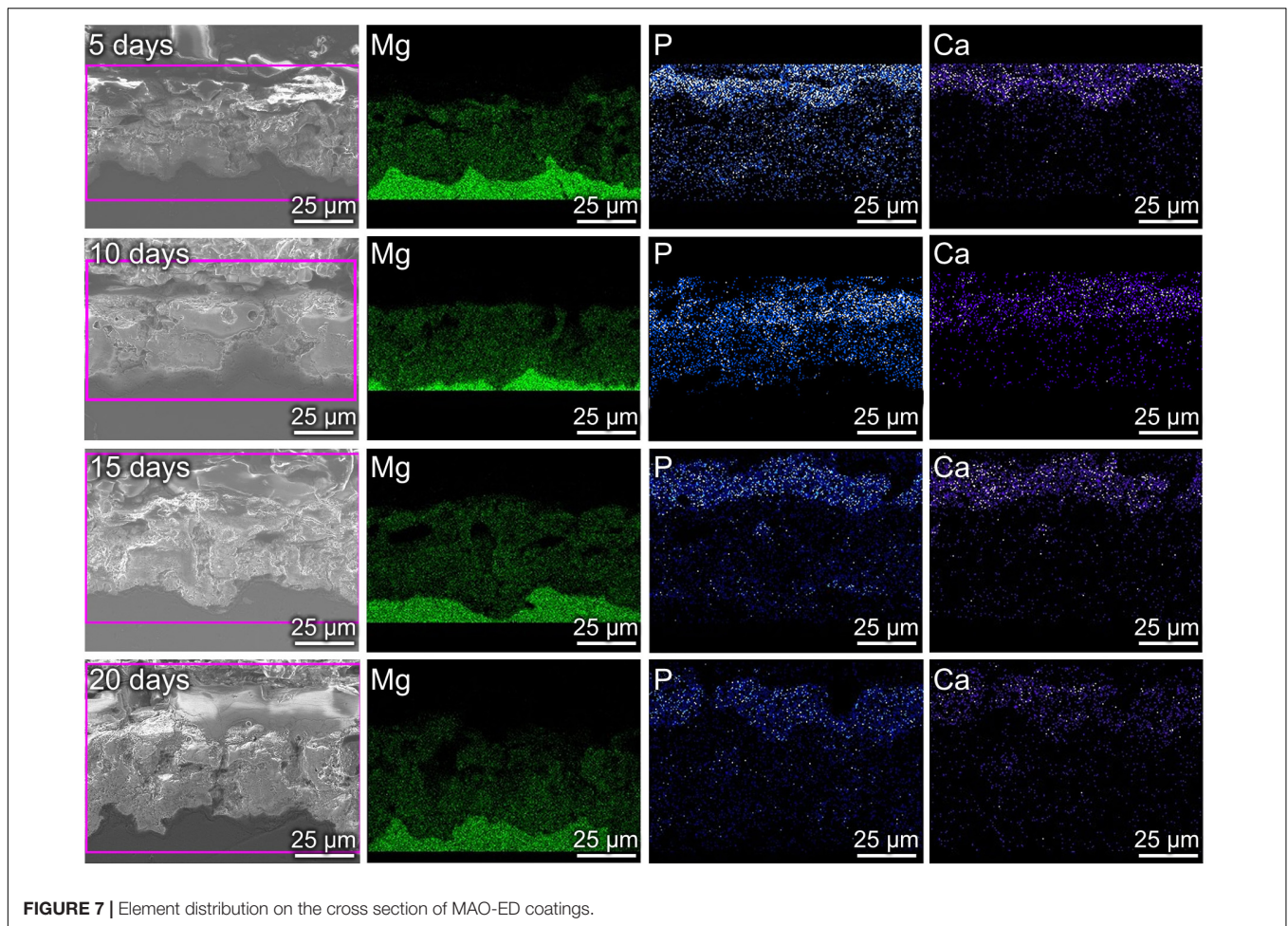


FIGURE 7 | Element distribution on the cross section of MAO-ED coatings.

on the implant material remains intact for the first 3–6 weeks, the chances of osseointegration will increase significantly (Song et al., 2010). Therefore, the deposition of the HA layer by MAO-ED technology is a reliable method to reduce degradation rate and improve biocompatibility of Mg alloys *in vivo*.

FT-IR Patterns

Figure 8 displays the infrared spectra of corrosion products deposited on the MAO-ED coating sample surface. No obvious change in the functional groups of corrosion products are observed during 20 days of immersion. The weak peak at 870 cm^{-1} belongs to the characteristic absorption of HPO_4^{2-} . Another two strong absorption peaks at 556 cm^{-1} and $1,055\text{ cm}^{-1}$ are assigned to the P-O stretching vibrations. According to the XRD spectra of the corrosion products, these types of functional groups are ascribed to $\text{Ca}_9\text{HPO}_4(\text{PO}_4)_5\text{OH}$ phase which decomposed from the HA layer. As the immersing time prolongs, the intensities of these peaks greatly decrease while their widths increase, indicating that $\text{Ca}_9\text{HPO}_4(\text{PO}_4)_5\text{OH}$ is gradually covered by the new sediments. New absorption peaks at $1,410$ and $1,647\text{ cm}^{-1}$ are respectively assigned to the C-O and C=O stretching vibrations, where the intensities of these two peaks increase with increasing time of immersion

(**Figure 8**). Based on the phase analysis, it can be considered that C mainly originates from the corrosion product $\text{CaMg}_3(\text{CO}_3)_4$ and it is presented in the form of carbonate on the sample surface. As shown in **Figure 8**, absorption peaks at $3,430\text{ cm}^{-1}$

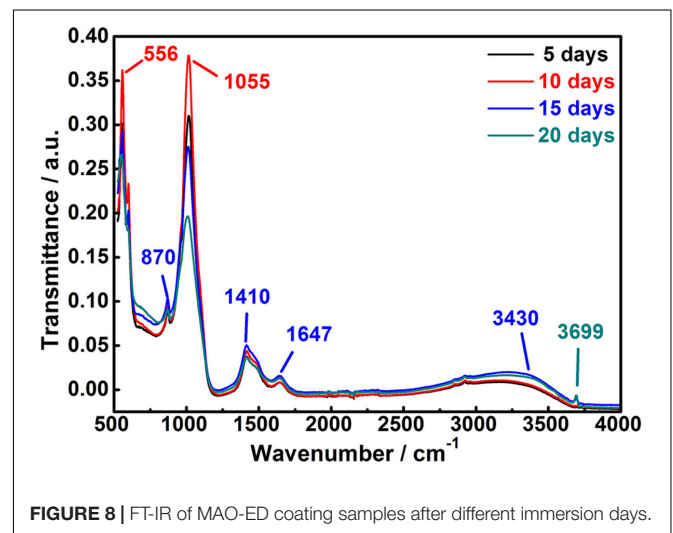


FIGURE 8 | FT-IR of MAO-ED coating samples after different immersion days.

are observed in all spectra, which are assigned to the absorption of O-H stretching vibration of corrosion products. As the immersion time prolongs, peaks at $3,430\text{ cm}^{-1}$ become more intense owing to the increase of O-H content. The intensities of peaks at $3,430\text{ cm}^{-1}$ increase, indicating that the content of HA synthesized on the sedimentary surface gradually increases during immersion.

Electrochemical Characteristics and Degradation Model of MAO-ED Coating in SBF

In order to deeply understand the degradation mechanism of MAO-ED coating in SBF solution, electrochemical impedance spectroscopy was conducted on the immersed samples with different days of immersion. **Figure 9** shows the Nyquist diagram and Bode diagram. **Table 5** lists the fitted results of EIS. Combining the results from **Figures 5, 7, 9**, a degradation model of MAO-ED coating in SBF is suggested based on the double-deck coating on Mg alloys (Li B. et al., 2014; Wang et al., 2019), which can be divided into three stages: deposition product formation stage, crack propagation stage and internal corrosion stage respectively (**Figure 10**). Fitted equivalent circuits of EIS data corresponding to the three stages are shown in **Figure 10**. In the equivalent circuits, R_s represents solution resistance, R_{cp} represents the deposition layer resistance, R_{ct} represents charge transfer resistance, R_h represents HA layer resistance, and R_m represents MAO coating resistance. The interpretation of **Figures 9, 10** and **Table 5** will be presented along with three stages of degradation model for MAO-ED coating immersed in SBF.

Deposition Product Formation Stage

The coating degradation model in SBF during the deposition product absorption stage (0- to 5-day immersion) is shown in **Figure 10a**. During immersion, SBF solution can only slowly penetrate the ED coating to finally reach the MAO coating. At the beginning of immersion, the HA layer firstly contacts SBF, leading to the decomposition of HA (Eqs 2 and 3). Afterward, Ca-P compounds are formed by the accumulation of Ca-P ions on the MAO-ED coating surface. After 5-days of immersion, the impedance arc of MAO-ED coating is the largest (as indicated by arrow in **Figure 9A**), which specifies that the MAO-ED coating of 5-day immersion has the highest impedance (as well as highest density) compared with other MAO-ED coatings with different immersion days. A uniform and dense layer is then deposited after 5-days of immersion, which is consistent with the morphologies shown in **Figures 5, 7**. Micro-cracks in the layer have not yet expanded and therefore the layer can still protect the substrate (**Figure 10a**). **Table 5** shows the fitting EIS results. The R_{cp} is relatively large after 5-days of immersion. Compared with other MAO-ED coatings with different immersion days, the R_{ct} value of the 5-day immersed sample indicates that there is no obvious interior corrosion. During this stage, absorption plays the dominant role in the product of deposition on the coating surface, so that the corrosion medium has difficulty penetrating into the coating through micro-cracks on the surface. From the analysis above, the deposition products of this stage contain HA and phosphates. Hence the Ca/P ratio of sample surface increases. It can be speculated that the biocompatibility and bone inductivity of MAO-ED coating can be effectively improved during the beginning stage of implantation.

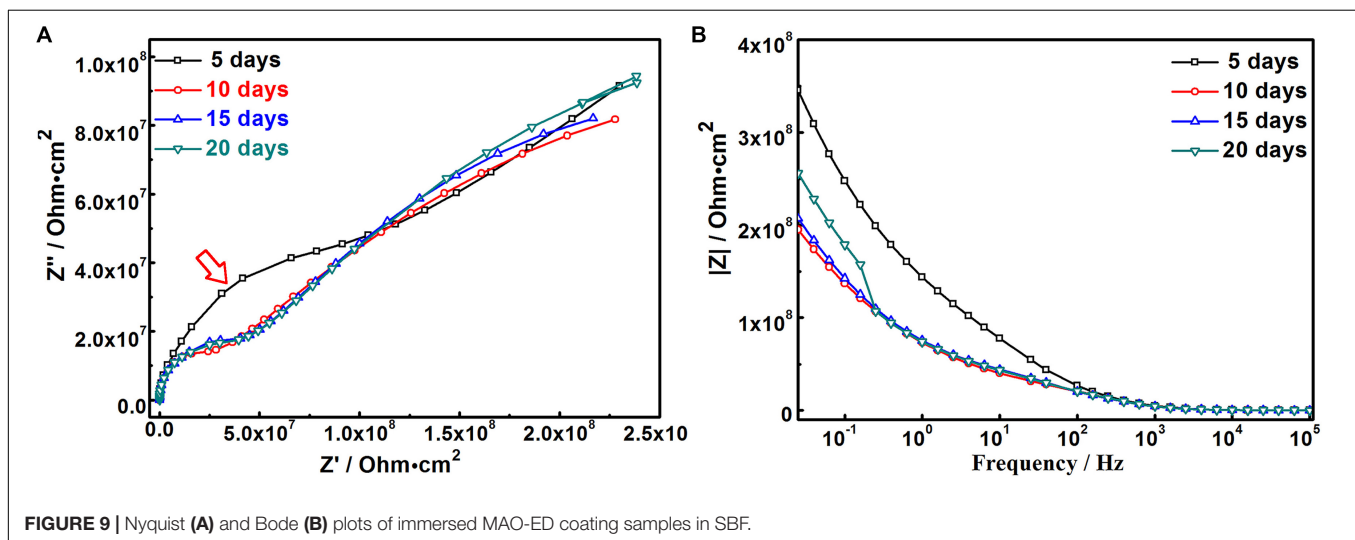
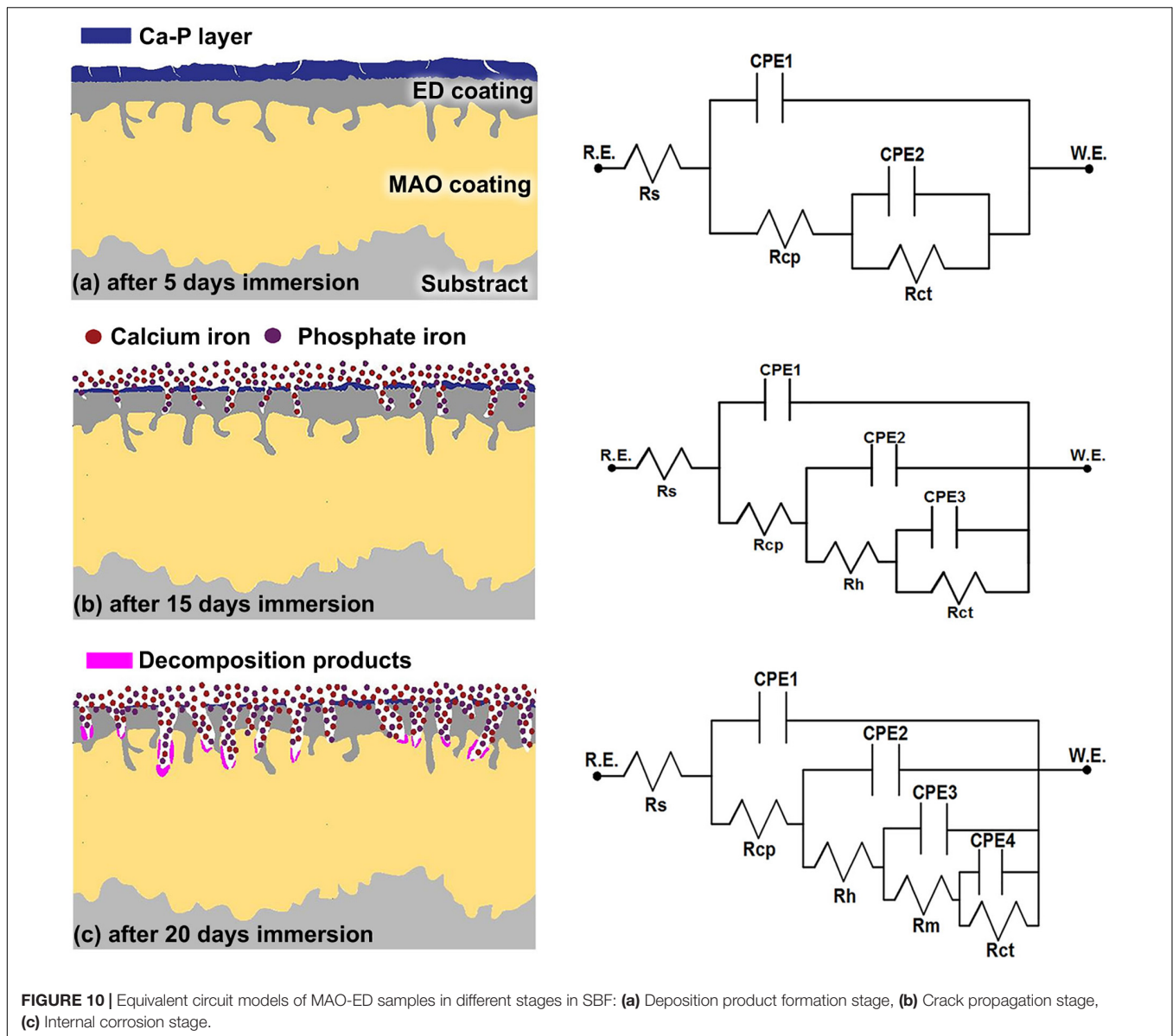


TABLE 5 | Fitting EIS data of MAO-ED samples in SBF after different immersion days.

Immersion time (days)	R_s ($\Omega\text{ cm}^2$)	R_{cp} ($\Omega\text{ cm}^2$)	R_h ($\Omega\text{ cm}^2$)	R_m ($\Omega\text{ cm}^2$)	R_{ct} ($\Omega\text{ cm}^2$)
5	53	7.45×10^3	–	–	6.99×10^4
10	48	9.06×10^3	2.44×10^3	–	4.34×10^4
15	59	5.13×10^3	3.87×10^3	1.57×10^3	2.11×10^4
20	72	2.21×10^3	1.03×10^3	1.06×10^3	1.03×10^4



Crack Propagation Stage

The coating degradation model of the crack propagation stage (5- to 15-day immersion) is shown in **Figure 10b**. As the immersion time prolongs, micro-cracks on the surface propagate due to the further corrosion by SBF. Based on the former analysis, the decomposition rates of HA are distinct in different areas, hence micro-cracks in some areas have propagated across the deposition product layer during this stage. As a result, SBF can permeate the ED coating (i.e., the electrophoretic deposited HA coating) through the micro-cracks, leading to the degradation of the ED coating. Therefore, the degradation rate gradually becomes higher than the deposition rate. According to the **Table 5**, the R_{ct} value decreases from $6.99 \times 10^4 \Omega \text{ cm}^2$ (5-day immersion) to $2.11 \times 10^4 \Omega \text{ cm}^2$ (15-day immersion) and the R_{cp} value of the deposition product layer also decreases obviously (**Table 5**). It indicates that micro-cracks accelerate the

corrosion of the deposition product layer and both the deposition product layer and the ED coating are degraded. Therefore, the degradation rate of the deposition product layer becomes higher. It can be seen from **Table 5** that the R_h value of the ED coating does not decrease during this stage, illustrating that the coating can still protect the Mg alloy substrate. The reason is that the ED coating can still induce the Ca and P from SBF to form deposits on the sample surface. Meanwhile, the degradation reactions are not strong enough to take the dominant place of deposition reactions.

Internal Corrosion Stage

The coating degradation model of the internal corrosion stage (after 15 days of immersion) is shown in **Figure 10c**. After 15 days of immersion, a large number of micro-pores are presented on the sample surface. Through-cracks and local peeling-off of ED

coating can also be observed on the cross-section morphologies (Figure 10c). ED coating gradually becomes porous and loose due to degradation. Consequently, SBF can easily reach and corrode the MAO coating and even the substrate. The amount of corrosion products [such as $\text{Mg}(\text{OH})_2$] and the pH value of the SBF solution gradually increase over immersion time. The degradation of the MAO coating gradually becomes dominant in this stage and the degradation behavior at micro-crack areas can be referred to the MAO coating degradation model in literature (Wang et al., 2018). The degradation model for MAO coating in SBF explains the degradation process and corrosion mechanism for the sample in different periods. In terms of the fitting results (Table 5), the values of R_h , R_m , and R_{cp} which represent the impedances of ED coating, the MAO coating and the deposition product layer, decrease. Especially, the R_{ct} value decreases to $1.03 \times 10^4 \Omega \text{ cm}^2$, indicating that the inner MAO coating is further corroded by the SBF solution.

CONCLUSION

In this work, ZK60 Mg alloy was micro-arc oxidized (MAO) and followed by electrophoretic deposition (ED) process. Both micro-arc oxidized coating samples with and without electrophoretic deposition treatment were investigated. After the examinations of microstructures, phase constituents, immersion tests and electrochemical measurements, some key points can be concluded as follows:

- (1) ED process applied to MAO coating can produce a flat and uniform hydroxyapatite (HA) layer, effectively covering the micro-pores and micro-cracks on the original MAO coating. Ca/P ratio of the MAO-ED coating surface reaches 1.60 which is close to the standard value (1.67) of implants. Meanwhile, the MAO-ED coating can be entirely wetted by water, indicating a nice biological performance to be used as implants.
- (2) The main deposition product of $\text{Ca}_9\text{HPO}_4(\text{PO}_4)_5\text{OH}$ at the beginning of immersion gradually changes to HA on the MAO-ED coating during the later immersion period,

indicating a good HA inducing ability of the coating and thereby a good potential biocompatibility. Deposition of Ca-P compounds and degradation of the coating take place simultaneously. When the degradation rate is higher than the deposition rate, degradation becomes the dominant reaction and the coating would gradually fail.

- (3) The degradation model of the composite coating is suggested to explain its degradation behavior at different stages during immersion in detail. It can be inferred that the degradation rate of the MAO-ED coating mainly depends on its ability for inducing Ca-P compounds and corrosion resistance.

DATA AVAILABILITY STATEMENT

The raw data supporting the conclusions of this article will be made available by the authors, without undue reservation.

AUTHOR CONTRIBUTIONS

Z-XW and LX conceived and designed the experiments. J-WZ, W-GL, and FY performed experiments. W-GL and CX analyzed the data. Z-XW, JY, and SL wrote the manuscript. All authors contributed to the article and approved the submitted version.

FUNDING

This research was funded by Postgraduate Research & Practice Innovation Program of Jiangsu Province KYCX18_2317.

ACKNOWLEDGMENTS

The authors would like to acknowledge Instrumental Analysis Center of Jiangsu University of Science and Technology for providing technology support.

REFERENCES

- Agarwal, S., Curtin, J., Duffy, B., and Jaiswal, S. (2016). Biodegradable magnesium alloys for orthopaedic applications: a review on corrosion, biocompatibility and surface modifications. *Mater. Sci. Eng. C* 68, 948–963. doi: 10.1016/j.msec.2016.06.020
- Agarwal, S., Riffault, M., Hoey, D., Duffy, B., Curtin, J., and Jaiswal, S. (2017). Biomimetic hyaluronic acid-lysozyme composite coating on AZ31 Mg alloy with combined antibacterial and osteoinductive activities. *ACS Biomater. Sci. Eng.* 3, 3244–3253. doi: 10.1021/acsbmaterials.7b00527
- Ataee, A., Li, Y., Song, G., and Wen, C. (2017). Metal scaffolds processed by electron beam melting for biomedical applications,” in *Metallic Foam Bone*, Chapter: 3, Ed. C. Wen (Amsterdam: Elsevier-Woodhead Publishing), 83–110. doi: 10.1016/B978-0-08-101289-5.00003-2
- Bakhsheshi-Rad, H. R., Hamzah, E., Daroonparvar, M., Ebrahimi-Kahrizsangi, R., and Medraj, M. (2014). In-vitro corrosion inhibition mechanism of fluorine-doped hydroxyapatite and brushite coated Mg-Ca alloys for biomedical applications. *Ceram. Int.* 40, 7971–7982. doi: 10.1016/j.ceramint.2013.12.147
- Bian, D., Deng, J., Li, N., Chu, X., Liu, Y., Li, W., et al. (2018). In Vitro and in Vivo Studies on Biomedical Magnesium Low-Alloying with Elements Gadolinium and Zinc for Orthopedic Implant Applications. *ACS Appl. Mater. Interfaces* 10, 4394–4408. doi: 10.1021/acsami.7b15498
- Bose, S., Tarafder, S., and Bandyopadhyay, A. (2015). Hydroxyapatite coatings for metallic implants. *Hydroxyapatite Biomed. Appl.* 2015, 143–157. doi: 10.1016/b978-1-78242-033-0.00007-9
- Burg, K. J. L., Porter, S., and Kellam, J. F. (2000). Biomaterial developments for bone tissue engineering. *Biomaterials* 21, 2347–2359. doi: 10.1016/S0142-9612(00)00102-102
- Chai, L., Chen, K., Zhi, Y., Murty, K. L., Chen, L. Y., and Yang, Z. (2018). Nanotwins induced by pulsed laser and their hardening effect in a Zr alloy. *J. Alloys Compd.* 748, 163–170. doi: 10.1016/j.jallcom.2018.03.126
- Chen, C., Tan, J., Wu, W., Petrini, L., Zhang, L., Shi, Y., et al. (2018). Modeling and Experimental Studies of Coating Delamination of Biodegradable Magnesium Alloy Cardiovascular Stents. *ACS Biomater. Sci. Eng.* 4, 3864–3873. doi: 10.1021/acsbmaterials.8b00700
- Chen, L. Y., Shen, P., Zhang, L., Lu, S., Chai, L., Yang, Z., et al. (2018). Corrosion behavior of non-equilibrium Zr-Sn-Nb-Fe-Cu-O alloys in high-temperature

- 0.01 M LiOH aqueous solution and degradation of the surface oxide films. *Corros. Sci.* 136, 221–230. doi: 10.1016/j.corsci.2018.03.012
- Chen, G., Guo, J., Nie, J., and Ma, G. (2016). Preparation, characterization, and application of PEO/HA core shell nanofibers based on electric field induced phase separation during electrospinning. *Polymer* 83, 12–19. doi: 10.1016/j.polymer.2015.12.002
- Chen, L., Zeng, Q., Li, J., Lu, J., Zhang, Y., Zhang, L. C., et al. (2016). Effect of microstructure on corrosion behavior of a Zr-Sn-Nb-Fe-Cu-O alloy. *Mater. Des.* 92, 888–896. doi: 10.1016/j.matdes.2015.12.067
- Chen, J., Lin, W., Liang, S., Zou, L., Wang, C., Wang, B., et al. (2019). Effect of alloy cations on corrosion resistance of LDH/MAO coating on magnesium alloy. *Appl. Surf. Sci.* 463, 535–544. doi: 10.1016/j.apsusc.2018.08.242
- Chen, L. Y., Wang, H., Zhao, C., Lu, S., Wang, Z. X., Sha, J., et al. (2019). Automatic remelting and enhanced mechanical performance of a plasma sprayed NiCrBSi coating. *Surf. Coatings Technol.* 369, 31–43. doi: 10.1016/j.surfcoat.2019.04.052
- Chen, L., Li, J., Zhang, Y., Zhang, L. C., Lu, W., Zhang, L., et al. (2015a). Effects of alloyed Si on the autoclave corrosion performance and periodic corrosion kinetics in Zr-Sn-Nb-Fe-O alloys. *Corros. Sci.* 100, 651–662. doi: 10.1016/j.corsci.2015.08.043
- Chen, L., Li, J., Zhang, Y., Zhang, L. C., Lu, W., Wang, L., et al. (2015b). Zr-Sn-Nb-Fe-Si-O alloy for fuel cladding candidate: processing, microstructure, corrosion resistance and tensile behavior. *Corros. Sci.* 100, 332–340. doi: 10.1016/j.corsci.2015.08.005
- Chen, X. M., Luo, C. P., and Liu, J. W. (2010a). Microstructure distribution of the micro-arc oxidizing coating on magnesium alloys. *J. Funct. Mater.* 41, 2075–2079.
- Chen, X. M., Luo, C. P., and Liu, J. W. (2010b). Study on the formation mechanism of micro-arc oxidation coatings on magnesium alloys. *Mater. Sci. Forum* 650, 228–233. doi: 10.4028/www.scientific.net/MSF.650.228
- Chen, Y., Zhang, J., Dai, N., Qin, P., Attar, H., and Zhang, L. C. (2017). Corrosion Behaviour of Selective Laser Melted Ti-TiB Biocomposite in Simulated Body Fluid. *Electrochim. Acta* 232, 89–97. doi: 10.1016/j.electacta.2017.02.112
- Cipriano, A. F., Lin, J., Lin, A., Sallee, A., Le, B., Cortez Alcaraz, M. C., et al. (2017). Degradation of Bioresorbable Mg-4Zn-1Sr intramedullary pins and associated biological responses in vitro and in vivo. *ACS Appl. Mater. Interfaces* 9, 44332–44355. doi: 10.1021/acsami.7b15975
- Gao, J. H., Guan, S. K., Chen, J., Wang, L. G., Zhu, S. J., Hu, J. H., et al. (2011). Fabrication and characterization of rod-like nano-hydroxyapatite on MAO coating supported on Mg-Zn-Ca alloy. *Appl. Surf. Sci.* 257, 2231–2237. doi: 10.1016/j.apsusc.2010.09.080
- García Rodenas, L., Palacios, J. M., Apella, M. C., Morando, P. J., and Blesa, M. A. (2005). Surface properties of various powdered hydroxyapatites. *J. Colloid Interface Sci.* 290, 145–154. doi: 10.1016/j.jcis.2005.04.041
- Gu, Y., Bandopadhyay, S., Chen, C. F., Guo, Y., and Ning, C. (2012). Effect of oxidation time on the corrosion behavior of micro-arc oxidation produced AZ31 magnesium alloys in simulated body fluid. *J. Alloys Compd.* 543, 109–117. doi: 10.1016/j.jallcom.2012.07.130
- Gu, Y., Bandopadhyay, S., Chen, C. F., Ning, C., and Guo, Y. (2013). Long-term corrosion inhibition mechanism of microarc oxidation coated AZ31 Mg alloys for biomedical applications. *Mater. Des.* 46, 66–75. doi: 10.1016/j.matdes.2012.09.056
- Habibovic, P., Barre, F., Van Blitterswijk, C. A., and De Groot, K. (2002). Biomimetic hydroxyapatite coating on metal implants. *J. Am. Ceram. Soc.* 85, 517–522. doi: 10.1111/j.1151-2916.2002.tb00126.x
- Han, B., Tang, B., and Nimni, M. E. (2003). Quantitative and sensitive in vitro assay for osteoinductive activity of demineralized bone matrix. *J. Orthop. Res.* 21, 648–654. doi: 10.1016/S0736-0266(03)00005-6
- Hornberger, H., Virtanen, S., and Boccaccini, A. R. (2012). Biomedical coatings on magnesium alloys - A review. *Acta Biomater.* 8, 2442–2455. doi: 10.1016/j.actbio.2012.04.012
- Ilich, J. Z., and Kerstetter, J. E. (2000). Nutrition in bone health revisited: a story beyond calcium. *J. Am. Coll. Nutr.* 19, 715–737. doi: 10.1080/07315724.2000.10718070
- Jia, Z. J., Li, M., Liu, Q., Xu, X. C., Cheng, Y., Zheng, Y. F., et al. (2014). Micro-arc oxidation of a novel Mg-1Ca alloy in three alkaline KF electrolytes: corrosion resistance and cytotoxicity. *Appl. Surf. Sci.* 292, 1030–1039. doi: 10.1016/j.apsusc.2013.11.038
- Jiang, S. T., Zhang, J., Shun, S. Z., and Chen, M. F. (2016). The formation of FHA coating on biodegradable Mg-Zn-Zr alloy using a two-step chemical treatment method. *Appl. Surf. Sci.* 388, 424–430. doi: 10.1016/j.apsusc.2015.12.087
- Kim, H. W., Koh, Y. H., Li, L. H., Lee, S., and Kim, H. E. (2004). Hydroxyapatite coating on titanium substrate with titania buffer layer processed by sol-gel method. *Biomaterials* 25, 2533–2538. doi: 10.1016/j.biomaterials.2003.09.041
- Li, B., Han, Y., and Qi, K. (2014). Formation mechanism, degradation behavior, and cytocompatibility of a nanorod-shaped HA and pore-sealed MgO bilayer coating on magnesium. *ACS Appl. Mater. Interfaces* 6, 18258–18274. doi: 10.1021/am505437e
- Li, Y., Lu, F., Li, H., Zhu, W., Pan, H., Tan, G., et al. (2014). Corrosion mechanism of micro-arc oxidation treated biocompatible AZ31 magnesium alloy in simulated body fluid. *Prog. Nat. Sci. Mater. Int.* 24, 516–522. doi: 10.1016/j.pnsc.2014.08.007
- Li, N., and Zheng, Y. (2013). Novel magnesium alloys developed for biomedical application: a review. *J. Mater. Sci. Technol.* 29, 489–502. doi: 10.1016/j.jmst.2013.02.005
- Liu, F., Xu, J., Wang, F., Zhao, L., and Shimizu, T. (2010). Biomimetic deposition of apatite coatings on micro-arc oxidation treated biomedical NiTi alloy. *Surf. Coatings Technol.* 204, 3294–3299. doi: 10.1016/j.surfcoat.2010.03.044
- Liu, G. Y., Tang, S., Li, D., and Hu, J. (2014). Self-adjustment of calcium phosphate coating on micro-arc oxidized magnesium and its influence on the corrosion behaviour in simulated body fluids. *Corros. Sci.* 79, 206–214. doi: 10.1016/j.corsci.2013.11.011
- Liu, J., Willför, S., and Xu, C. (2015). A review of bioactive plant polysaccharides: biological activities, functionalization, and biomedical applications. *Bioact. Carbohydrates Diet. Fibre* 5, 31–61. doi: 10.1016/j.bcdf.2014.12.001
- Luo, H., Cai, Q., Wei, B., Yu, B., Li, D., He, J., et al. (2008). Effect of (NaPO₃)₆ concentrations on corrosion resistance of plasma electrolytic oxidation coatings formed on AZ91D magnesium alloy. *J. Alloys Compd.* 464, 537–543. doi: 10.1016/j.jallcom.2007.10.072
- McEntire, B. J., Bal, B. S., Rahaman, M. N., Chevalier, J., and Pezzotti, G. (2015). Ceramics and ceramic coatings in orthopaedics. *J. Eur. Ceram. Soc.* 35, 4327–4369. doi: 10.1016/j.jeurceramsoc.2015.07.034
- Meng, E. C., Guan, S. K., Wang, H. X., Wang, L. G., Zhu, S. J., Hu, J. H., et al. (2011). Effect of electrodeposition modes on surface characteristics and corrosion properties of fluorine-doped hydroxyapatite coatings on Mg-Zn-Ca alloy. *Appl. Surf. Sci.* 257, 4811–4816. doi: 10.1016/j.apsusc.2010.12.073
- Pan, H., Kang, R., Li, J., Xie, H., Zeng, Z., Huang, Q., et al. (2020). Mechanistic investigation of a low-alloy Mg-Ca-based extrusion alloy with high strength-ductility synergy. *Acta Mater.* 186, 278–290. doi: 10.1016/j.actamat.2020.01.017
- Pan, H., Qin, G., Huang, Y., Ren, Y., Sha, X., Han, X., et al. (2018). Development of low-alloyed and rare-earth-free magnesium alloys having ultra-high strength. *Acta Mater.* 149, 350–363. doi: 10.1016/j.actamat.2018.03.002
- Pan, H., Yang, C., Yang, Y., Dai, Y., Zhou, D., Chai, L., et al. (2019). Ultra-fine grain size and exceptionally high strength in dilute Mg-Ca alloys achieved by conventional one-step extrusion. *Mater. Lett.* 237, 65–68. doi: 10.1016/j.matlet.2018.11.080
- Pan, L., and Yoon, R. H. (2018). Effects of electrolytes on the stability of wetting films: implications on seawater flotation. *Miner. Eng.* 122, 1–9. doi: 10.1016/j.mineng.2018.03.011
- Peng, F., Li, H., Wang, D., Tian, P., Tian, Y., Yuan, G., et al. (2016). Enhanced Corrosion Resistance and Biocompatibility of Magnesium Alloy by Mg-Al-Layered double hydroxide. *ACS Appl. Mater. Interfaces* 8, 35033–35044. doi: 10.1021/acsami.6b12974
- Pezzato, L., Brunelli, K., Napolitani, E., Magrini, M., and Dabalà, M. (2015). Surface properties of AZ91 magnesium alloy after PEO treatment using molybdate salts and low current densities. *Appl. Surf. Sci.* 357, 1031–1039. doi: 10.1016/j.apsusc.2015.09.107
- Qin, H., Zhao, Y., An, Z., Cheng, M., Wang, Q., Cheng, T., et al. (2015). Enhanced antibacterial properties, biocompatibility, and corrosion resistance of degradable Mg-Nd-Zn-Zr alloy. *Biomaterials* 53, 211–220. doi: 10.1016/j.biomaterials.2015.02.096
- Qin, P., Chen, Y., Liu, Y. J., Zhang, J., Chen, L. Y., Li, Y., et al. (2019). Resemblance in Corrosion Behavior of Selective Laser Melted and Traditional Monolithic β Ti-24Nb-4Zr-8Sn Alloy. *ACS Biomater. Sci. Eng.* 5, 1141–1149. doi: 10.1021/acsbmaterials.8b01341

- Qin, X., Guo, X., Lu, J., Chen, L., Qin, J., and Lu, W. (2017). Erosion-wear and intergranular corrosion resistance properties of AISI 304L austenitic stainless steel after low-temperature plasma nitriding. *J. Alloys Compd.* 698, 1094–1101. doi: 10.1016/j.jallcom.2016.12.164
- Rabadia, C. D., Liu, Y. J., Chen, L. Y., Jawed, S. F., Wang, L. Q., Sun, H., et al. (2019). Deformation and strength characteristics of Laves phases in titanium alloys. *Mater. Des.* 179:107891. doi: 10.1016/j.matdes.2019.107891
- Razavi, M., Fathi, M., Savabi, O., Vashae, D., and Tayebi, L. (2014). Improvement of biodegradability, bioactivity, mechanical integrity and cytocompatibility behavior of biodegradable mg based orthopedic implants using nanostructured Bredigite (Ca7MgSi4O16) Bioceramic Coated via ASD/EPD technique. *Ann. Biomed. Eng.* 42, 2537–2550. doi: 10.1007/s10439-014-1084-7
- Razavi, M., Fathi, M., Savabi, O., Vashae, D., and Tayebi, L. (2015). In vivo assessments of bioabsorbable AZ91 magnesium implants coated with nanostructured fluoridated hydroxyapatite by MAO/EPD technique for biomedical applications. *Mater. Sci. Eng. C* 48, 21–27. doi: 10.1016/j.msec.2014.11.020
- Sang, P., Chen, L. Y., Zhao, C., Wang, Z. X., Wang, H., Lu, S., et al. (2019). Particle size-dependent microstructure, hardness and electrochemical corrosion behavior of atmospheric plasma sprayed niCrbsi coatings. *Metals* 9:1342. doi: 10.3390/met9121342
- Sankara Narayanan, T. S. N., Park, I. S., and Lee, M. H. (2014). Strategies to improve the corrosion resistance of microarc oxidation (MAO) coated magnesium alloys for degradable implants: prospects and challenges. *Prog. Mater. Sci.* 60, 1–71. doi: 10.1016/j.pmatsci.2013.08.002
- Serre, C. M., Papillard, M., Chavassieux, P., Voegel, J. C., and Boivin, G. (1998). Influence of magnesium substitution on a collagen-apatite biomaterial on the production of a calcifying matrix by human osteoblasts. *J. Biomed. Mater. Res.* 42, 626–633. doi: 10.1002/(sici)1097-4636(19981215)42:4<626::aid-jbm20>3.0.co;2-s
- Shadanbaz, S., and Dias, G. J. (2012). Calcium phosphate coatings on magnesium alloys for biomedical applications: a review. *Acta Biomater.* 8, 20–30. doi: 10.1016/j.actbio.2011.10.016
- Song, Y., Zhang, S., Li, J., Zhao, C., and Zhang, X. (2010). Electrodeposition of Ca-P coatings on biodegradable Mg alloy: in vitro biomineralization behavior. *Acta Biomater.* 6, 1736–1742. doi: 10.1016/j.actbio.2009.12.020
- Suchanek, W., and Yoshimura, M. (1998). Processing and properties of hydroxyapatite-based biomaterials for use as hard tissue replacement implants. *J. Mater. Res.* 13, 94–117. doi: 10.1557/JMR.1998.0015
- Tampieri, A., Celotti, G., Sprio, S., Delcogliano, A., and Franzese, S. (2001). Porosity-graded hydroxyapatite ceramics to replace natural bone. *Biomaterials* 22, 1365–1370. doi: 10.1016/S0142-9612(00)00290-298
- Wang, Y., Li, X., Chen, M., Zhao, Y., You, C., Li, Y., et al. (2019). In Vitro and in Vivo Degradation Behavior and Biocompatibility Evaluation of Microarc Oxidation-Fluorinated Hydroxyapatite-Coated Mg-Zn-Zr-Sr Alloy for Bone Application. *ACS Biomater. Sci. Eng.* 5, 2858–2876. doi: 10.1021/acsbomaterials.9b00564
- Wang, Z. X., Chen, G. Q., Chen, L. Y., Xu, L., and Lu, S. (2018). Degradation behavior of micro-arc oxidized ZK60 magnesium alloy in a simulated body fluid. *Metals* 8, 1–17. doi: 10.3390/met8090724
- Xia, X., Zhao, Q., Peng, Y., Zhang, P., Liu, L., Ding, J., et al. (2020). Precipitation behavior and mechanical performances of A356.2 alloy treated by Al-Sr-La composite refinement-modification agent. *J. Alloys Compd.* 818:153370. doi: 10.1016/j.jallcom.2019.153370
- Xiong, Y., Hu, X., and Song, R. (2017). Characteristics of CeO2/ZrO2-HA composite coating on ZK60 magnesium alloy. *J. Mater. Res.* 32, 1073–1082. doi: 10.1557/jmr.2017.48
- Xiong, Y., Lu, C., Wang, C., and Song, R. (2014). The n-MAO/EPD bio-ceramic composite coating fabricated on ZK60 magnesium alloy using combined micro-arc oxidation with electrophoretic deposition. *Appl. Surf. Sci.* 322, 230–235. doi: 10.1016/j.apsusc.2014.10.103
- Yanovska, A., Kuznetsov, V., Stanislavov, A., Danilchenko, S., and Sukhodub, L. (2012). Calcium-phosphate coatings obtained biomimetically on magnesium substrates under low magnetic field. *Appl. Surf. Sci.* 258, 8577–8584. doi: 10.1016/j.apsusc.2012.05.052
- Yazdimamaghani, M., Razavi, M., Vashae, D., and Tayebi, L. (2015). Surface modification of biodegradable porous Mg bone scaffold using polycaprolactone/bioactive glass composite. *Mater. Sci. Eng. C* 49, 436–444. doi: 10.1016/j.msec.2015.01.041
- Zhang, L. C., and Chen, L. Y. (2019). A review on biomedical titanium alloys: recent progress and prospect. *Adv. Eng. Mater.* 21:1801215. doi: 10.1002/adem.201801215
- Zhang, L. C., Chen, L. Y., and Wang, L. (2020). Surface modification of titanium and titanium alloys: technologies, developments, and future interests. *Adv. Eng. Mater.* 22:1901258. doi: 10.1002/adem.201901258
- Zhang, L. C., Jia, Z., Lyu, F., Liang, S. X., and Lu, J. (2019). A review of catalytic performance of metallic glasses in wastewater treatment: recent progress and prospects. *Prog. Mater. Sci.* 105:100576. doi: 10.1016/j.pmatsci.2019.100576
- Zhang, L., Chen, L. Y., Zhao, C., Liu, Y., and Zhang, L. C. (2019). Calculation of oxygen diffusion coefficients in oxide films formed on low-temperature annealed Zr alloys and their related corrosion behavior. *Metals* 9:850. doi: 10.3390/met9080850
- Zhang, Y. M., Chen, L. Y., Lu, S., Zhao, C., and Wang, Y. H. (2019). Refined microstructure and enhanced hardness in friction stir-welded AZ31 magnesium alloy induced by heat pipe with different cooling liquid. *Metals* 9:1227. doi: 10.3390/met9111227
- Zhang, L. C., Xu, J., and Ma, E. (2006a). Consolidation and properties of ball-milled Ti50Cu18Ni22Al4 Sn6 glassy alloy by equal channel angular extrusion. *Mater. Sci. Eng. A* 434, 280–288. doi: 10.1016/j.msea.2006.06.085
- Zhang, L. C., Xu, J., and Eckert, J. (2006b). Thermal stability and crystallization kinetics of mechanically alloyed TiC/Ti-based metallic glass matrix composite. *J. Appl. Phys.* 100:033514. doi: 10.1063/1.2234535
- Zhao, X., Shi, L. L., and Xu, J. (2013). Mg-Zn-Y alloys with long-period stacking ordered structure: in vitro assessments of biodegradation behavior. *Mater. Sci. Eng. C* 33, 3627–3637. doi: 10.1016/j.msec.2013.04.051
- Zheng, Y., Lai, L., Liu, W., Jiang, H., and Wang, X. (2017). Recent advances in biomedical applications of fluorescent gold nanoclusters. *Adv. Colloid Interface Sci.* 242, 1–16. doi: 10.1016/j.cis.2017.02.005
- Zhou, X., Thompson, G. E., Skeldon, P., Wood, G. C., Shimizu, K., and Habazaki, H. (1999). Film formation and detachment during anodizing of Al-Mg alloys. *Corros. Sci.* 41, 1599–1613. doi: 10.1016/S0010-938X(99)00007-4
- Zhu, D., Su, Y., Young, M. L., Ma, J., Zheng, Y., and Tang, L. (2017). Biological responses and mechanisms of human bone marrow mesenchymal stem cells to Zn and Mg biomaterials. *ACS Appl. Mater. Interfaces* 9, 27453–27461. doi: 10.1021/acscami.7b06654

Conflict of Interest: W-G.L. was employed by the company Zhenjiang Naisi Advanced Materials Co., Ltd.

The remaining authors declare that the research was conducted in the absence of any commercial or financial relationships that could be construed as a potential conflict of interest.

Copyright © 2020 Wang, Xu, Zhang, Ye, Lv, Xu, Lu and Yang. This is an open-access article distributed under the terms of the Creative Commons Attribution License (CC BY). The use, distribution or reproduction in other forums is permitted, provided the original author(s) and the copyright owner(s) are credited and that the original publication in this journal is cited, in accordance with accepted academic practice. No use, distribution or reproduction is permitted which does not comply with these terms.